Supporting Information for

Confinement-modulated Phase Transition of Fe-Ni Melt in Carbon Nanotube

Qingshui Liu[1], Wenhui Fang[1], Mengshuang Fu[1], Quhan Lv[1], Lishu Zhang[*,1], Weikang Wu[*,1], Hui Li[*,1]

[1]*Key Laboratory for Liquid-Solid Structural Evolution and Processing of Materials, Ministry of Education, Shandong University, Jinan 250061, China*

* Corresponding author:

Lishu Zhang: lishu.zhang@sdu.edu.cn

Weikang Wu: weikang_wu@sdu.edu.cn

Hui Li: lihuilmy@hotmail.com

1. Robustness of structural features with respect to interatomic potentials

To evaluate the robustness of the identified structural features, we systematically examined the sensitivity of (i) the optimal density, (ii) CNS population evolution, and (iii) phase boundaries using different Fe–Ni empirical potentials and metal–carbon interaction parameters.

S1.1 Robustness of the optimal density (~7 g/cm³)

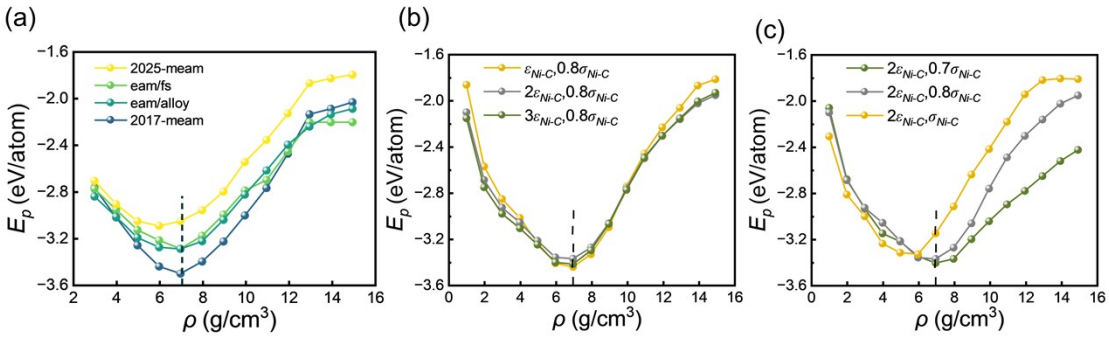

Figure S1. (a) Potential energy E_p as a function of density under different Fe–Ni empirical potentials (2025-MEAM, EAM/FS, EAM/alloy, and 2017-MEAM); (b) $E_p$as a function of density with varying $\varepsilon_{Ni\text{-}C}$ at fixed $\sigma_{Ni\text{-}C}$; (c) E_p as a function of density with varying $\sigma_{Ni\text{-}C}$ at fixed $\varepsilon_{Ni\text{-}C}$.

The potential energy Ep as a function of density was calculated using several Fe–Ni empirical potentials (2025-MEAM, EAM/FS, EAM/alloy, and 2017-MEAM), together with a series of Lennard–Jones (LJ) parameter variations for metal–carbon interactions. Specifically, $\varepsilon_{Fe\text{–}C}$ and $\sigma_{Fe\text{–}C}$ were fixed, while $\varepsilon_{Ni\text{–}C}$ and $\sigma_{Ni\text{–}C}$ were systematically varied (**see Table S1**).

Table S1. LJ parameters for metal–carbon interactions. (i,j) denotes the scaling factors for $\varepsilon_{Ni\text{-}C}$ and $\sigma_{Ni\text{-}C}$, respectively, while Fe–C parameters are fixed.

Parameter set (i,j)	$\varepsilon_{Ni\text{-}C}$ (eV)	$\sigma_{Ni\text{-}C}$ (Å)	$\varepsilon_{Fe\text{-}C}$ (eV)	$\sigma_{Fe\text{-}C}$ (Å)
(1,1)	0.023	2.852		
(1,0.8)	0.023	2.282	0.044	2.221
(2,0.8)	0.046	2.282		

(2,0.7)	0.046	1.997
(3,0.8)	0.069	2.282
(2,1)	0.046	2.852

As shown in **Fig. S1(a–c)**, although different potentials lead to variations in the absolute values of the potential energy, all E_p–ρ curves exhibit a consistent "U"-shaped dependence, with the minimum located near $\rho \approx 7$ g/cm^3. This result demonstrates that the optimal density is essentially insensitive to both the choice of Fe–Ni potential and reasonable variations in LJ parameters, indicating that it is an intrinsic property of the confined system.

1.2 Robustness of CNS oscillatory behavior

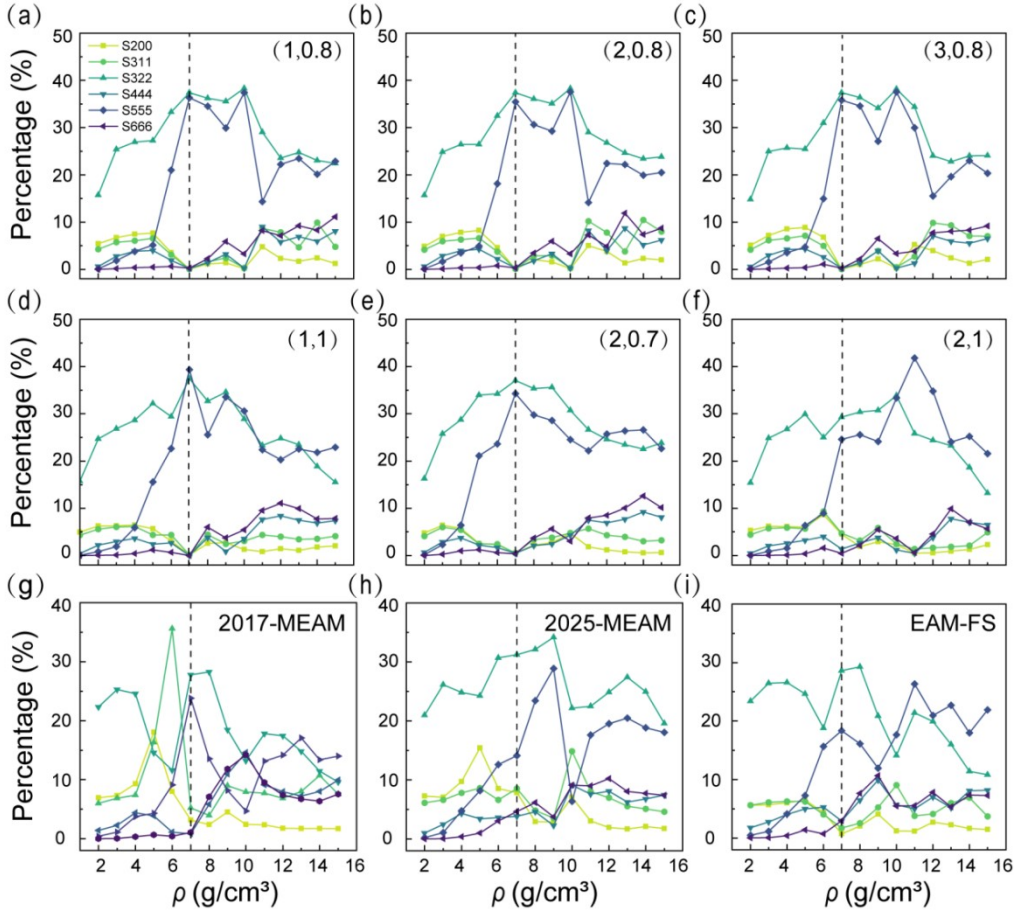

Figure S2. Density dependence of CNS percentages under different Lennard -Jones (LJ) parameter sets and Fe-Ni potentials: (a) (1,0.8), (b) (2,0.8), (c) (3,0.8), (d) (1,1), (e) (2,0.7), (f) (2,1); (g) 2017-MEAM, (h) 2025-MEAM, and (i) EAM/FS.

The density dependence of CNS populations under different LJ parameter sets and Fe–Ni potentials is shown in **Fig. S2**. Despite quantitative differences, the

qualitative behavior remains highly consistent across all cases.

Specifically, CNS populations exhibit a pronounced oscillatory dependence on density. The first group (S555 and S322) shows maxima near ~7 g/cm³, whereas the second group (S200, S311, S444, and S666) exhibits corresponding minima. Moreover, these two groups display anti-correlated evolution over the same density range, indicating competitive structural transformation.

Although the exact positions of extrema vary slightly with parameter choice, the oscillatory behavior and the associated competition mechanism remain unchanged. This consistency indicates that the CNS evolution reflects an intrinsic structural response to confinement-induced densification, rather than an artifact of the interatomic potential.

1.3 Robustness of phase boundaries

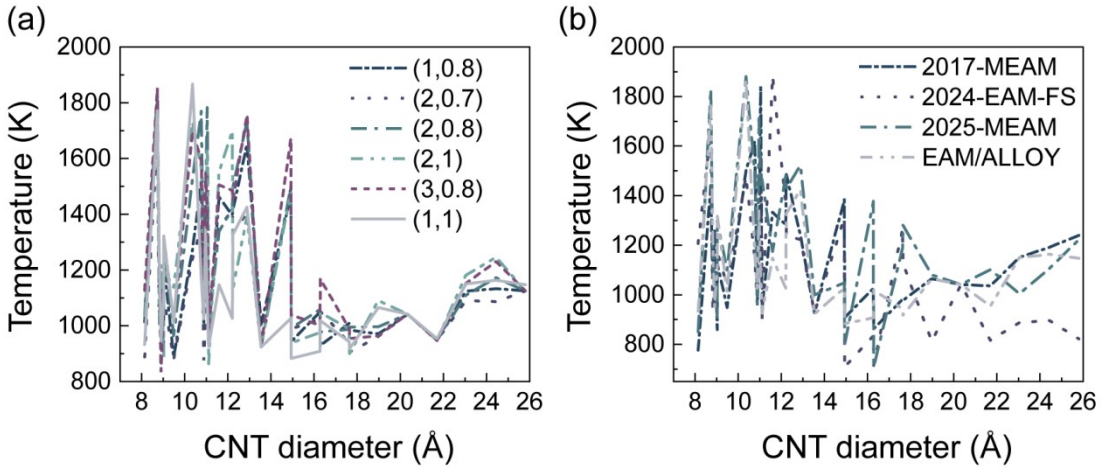

Figure S3. Sensitivity of phase boundaries to interatomic potentials. (a) Transition temperature as a function of CNT diameter under different Lennard–Jones (LJ) parameter sets ($i\varepsilon_{Ni\text{-}C}$, $j\sigma_{Ni\text{-}C}$); (b) transition temperature as a function of CNT diameter predicted by different Fe–Ni empirical potentials (2017-MEAM, 2024-EAM/FS, 2025-MEAM, and EAM/alloy).

The sensitivity of phase boundaries to interatomic potentials is presented in **Fig. S3**. While different potentials result in quantitative variations in transition temperatures, the overall dependence of phase boundaries on CNT diameter remains consistent.

All potentials predict similar fluctuation patterns and comparable transition regimes, indicating that the phase boundary behavior is not qualitatively sensitive to the specific Fe–Ni potential. This suggests that the phase transitions are primarily governed by geometric confinement and atomic packing constraints, rather than fine details of interatomic interactions.

In addition, the EAM/alloy potential has been extensively validated for Fe–Ni systems, as it reliably reproduces thermodynamic properties, defect energetics, and experimental phase diagrams. Its widespread application in simulations of mechanical behavior, cluster structures, and irradiation effects further supports its suitability for the present study.

1.4 Summary

Overall, the optimal density (~7 g/cm³), the oscillatory evolution of CNS populations, and the phase boundary characteristics all exhibit strong robustness with respect to reasonable variations in interatomic potentials. These results confirm that the key findings of this work originate from intrinsic geometric confinement and density-induced structural crossover, rather than from specific potential parameterizations.

2. Solidification behavior under bulk, free-standing, and confined conditions

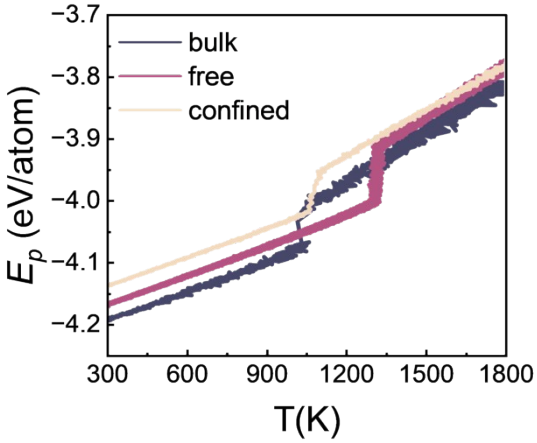

Figure S4. (a) The temperature dependence of the potential energy(E_p) for bulk, free-standing and confined FeNi alloy melt encapsulated in (24,24) CNT.

Fig. S4 shows the potential energy as a function of temperature during solidification at a cooling rate of 0.1 k/ps for bulk, free-standing nanowire, and confined nanowire encapsulated in (24,24) CNT. The transition point in potential energy corresponds to the solidification transition temperature (T_S). The free-standing nanowire, confined nanowire and bulk solidify at approximately 1304K, 1108K, and

1021K, respectively. The Ts of confined nanowire is higher than that of bulk counterparts due to the CNT serve as a “foreign” surface in heterogeneous nucleation, which reduces the nucleation work and the free energy barrier of nucleation, thereby facilitating solidification at higher temperatures. Conversely, the Ts of confined nanowire is lower than that of free-standing nanowires, because the CNTs decrease the large specific surface area, enhancing the thermal stability of the nanowires and delaying the solidification process.

3. Evolution of LaSCs

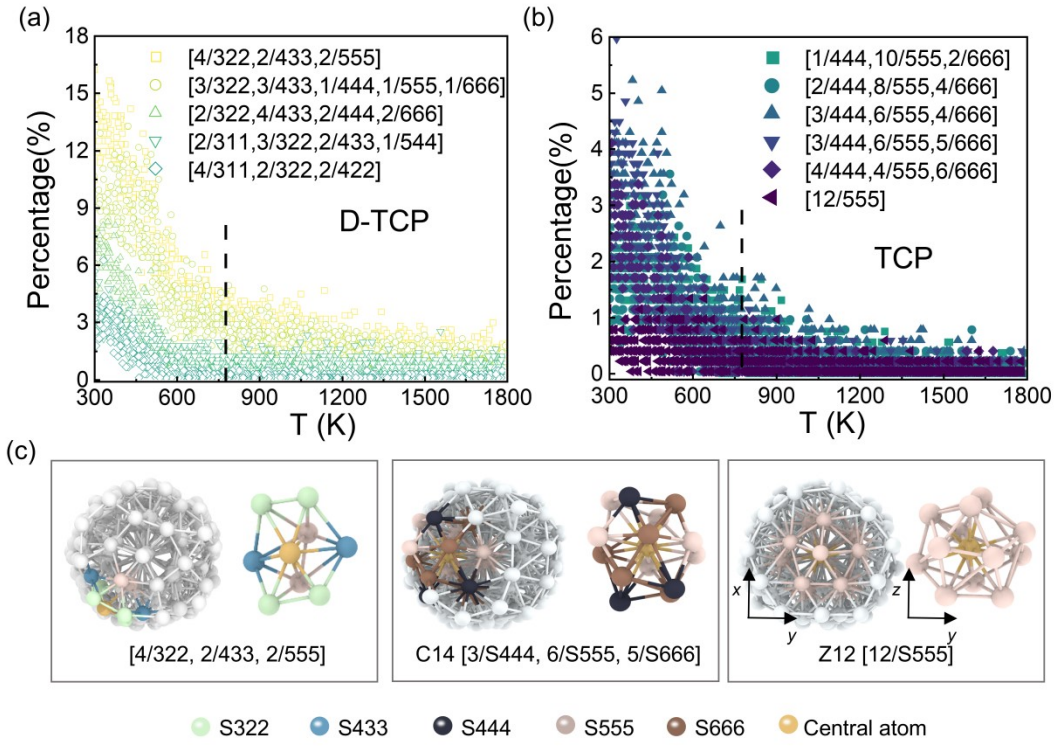

Figure S5.(a,b) The percentage of the top five D-TCPs LaSCs and the top six TCP LaSCs as a function of temperature during solidification, The dashed line indicates the glass transition temperature (Tg).(c) Top and side views of three representative LaSCs, whose central atoms are located in the outer, intermediate, and inner layers, respectively.

Fig. S5(a,b) illustrates the temperature dependence of five representative detective-TCP (D-TCP) LaSCs, namely [4/322, 2/433, 2/555], [2/322, 4/433, 2/444, 2/666], [3/322, 3/433, 1/444, 1/555, 1/666], [4/311, 2/322, 2/422], and [2/311, 3/322, 2/433, 1/544], as well as six typical TCP LaSCs (A13, B14, C13, C14, D14, and Z12).

When T>Tg, the percentage of LaSCs increases slowly; as the temperature approaches the glass transition temperature (Tg), the growth rate becomes significantly enhanced.

At 300 K, the percentage of D-TCPs is notably higher than that of TCPs. This can be attributed to the radial inhomogeneity of atomic distribution in the nanowire, where the outer layer contains more atoms than the middle layer, and the middle layer more than the inner layer. Due to the absence of complete radial nearest-neighbor coordination (i.e., missing radial ligand atoms) in the outer layer, the effective cluster size is reduced (typically 8–10 atoms), leading to symmetry breaking and the formation of D-TCPs, such as [4/322, 2/433, 2/555] (see **Fig. S5(c)**). By contrast, when the central atom is located in the middle or inner layer, a more complete coordination environment can be established, favoring the formation of higher-symmetry TCP structures. For example, structures such as C14 tend to form when the central atom is located in the middle layer, while highly symmetric Z12 structures can only form when the central atom resides in the inner layer, where sufficient radial nearest neighbors are available.

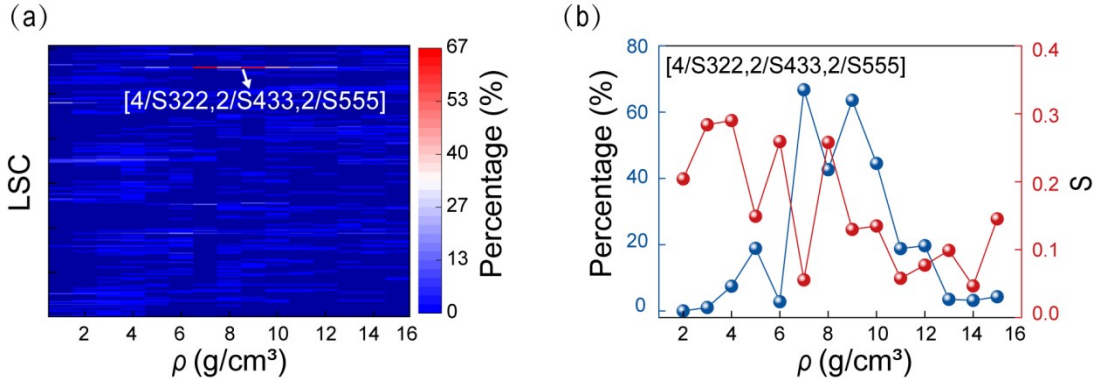

Figure S6. (a) Heat map showing the percentage of 206 types of Largest Standard Clusters at different densities. (b) Percentage and *S* of the [4/S322, 2/S433, 2/S555] clusters as a function of density.

Fig. S6(a) presents a heat map showing the fraction of 206 types of Largest Standard Clusters (LaSCs) at different densities. Among them, the [4/S322, 2/S433, 2/S555] LaSC maintains a relatively high proportion across the entire density range, indicating that it is representative of the structural evolution.

Fig. S6(b) shows the fraction and sphericity parameter *S* of the [4/S322, 2/S433,

2/S555] cluster as a function of density. The results indicate that this cluster exhibits minimal distortion at approximately 7 g/cm³. Since it is composed of three CNS types (S322, S433, and S555), the low distortion of this LaSC reflects the reduced distortion of its constituent CNSs at the same density.

4. Mechanical analysis

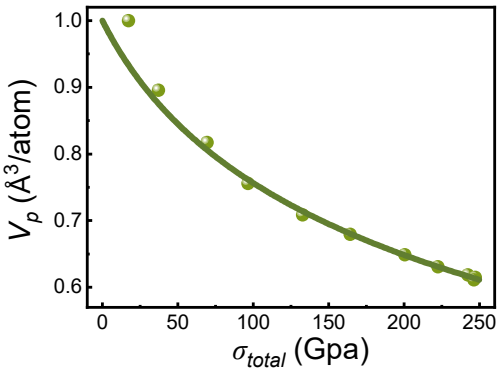

Figure S7. Volume per atom (V_p) as function of total stress (σ_{total}).

An intrinsic mechanical analysis of the densification region reveals that the V_p-σ_{total} relationship can be accurately fitted by the third-order Birch–Murnaghan equation of state (BM-EOS), yielding B_0= 221.9 ± 3.6 GPa and B′=3.5±0.2, which is significantly higher than that of typical FeNi-based metallic glasses (160–170 GPa). Moreover, the BM-EOS curve is continuous and smooth, with no abrupt volume changes or compression anomalies, indicating that no structural phase transition occurred throughout the densification process. Therefore, the potential energy minimum at 7 g/cm³ should be attributed to structural regulation mechanisms rather than a amorphous–amorphous phase transitions.

5. Origin of CNS oscillations

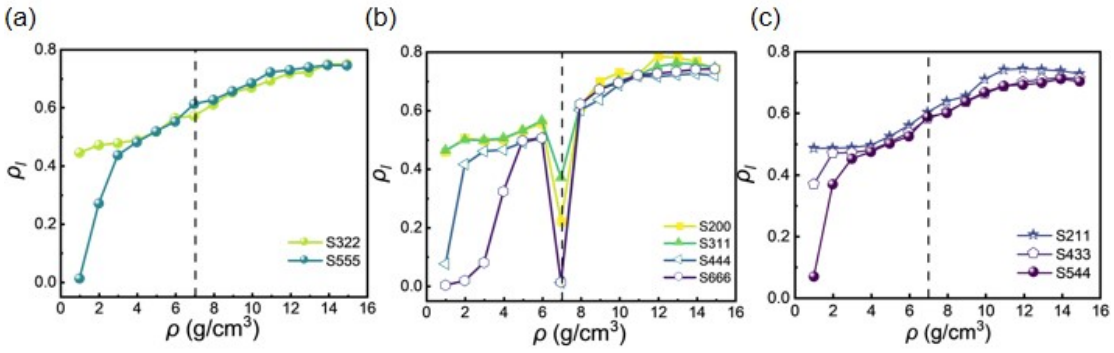

Figure S8. Local packing efficiency (ρ_l) of different CNS types with density: (a,d) S555 and S322; (b,e) S200, S311, S444, and S666; (c,f) S211, S433, and S544.

Fig.S8 shows that the local packing efficiency (ρ_l) of the main CNS. The results indicate that ρ_l generally increases with density, while the differences among CNS types remain relatively small. Therefore, packing efficiency alone cannot account for the observed oscillatory behavior.

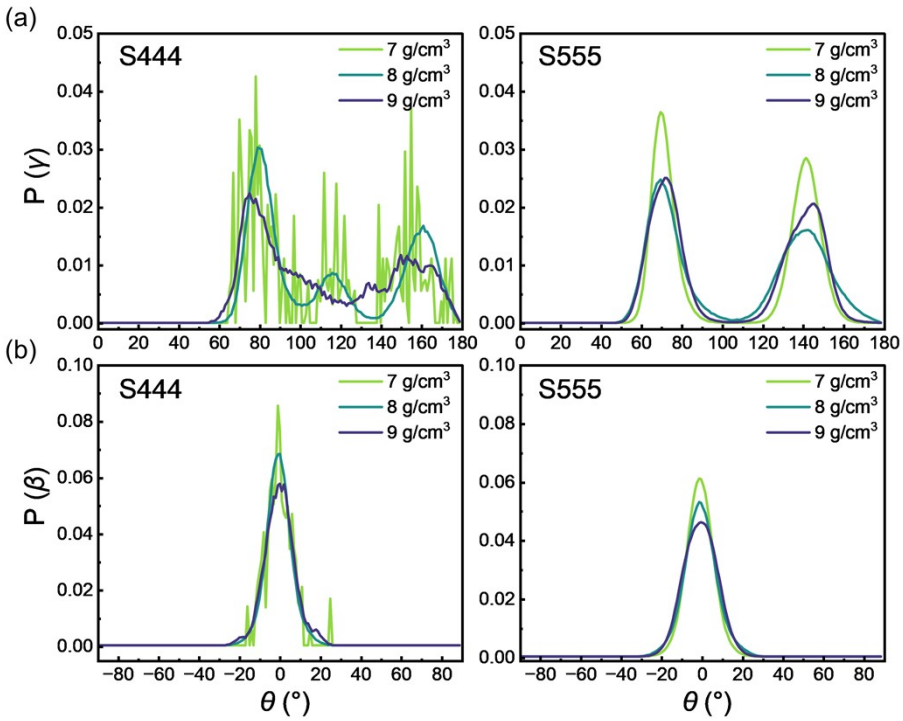

Figure S9. Angular distributions of S444 and S555 at three densities (7, 8, and 9 g/cm³): (a, b) P(γ), and (c, d) P(β).

To further explore the physical origin of the fluctuations in CNS fractions, we proceed to analyze the confinement-induced strain.Taking S444 and S555 as representative examples, we calculated the probability density distributions of the characteristic angles γ and β, namely P(γ) and P(β), at densities of 7, 8, and 9 g/cm³.

Sharper peaks indicate the lower structural distortion.

The results show that in the P(γ) distributions, the in-plane distortion of both S444 and S555 exhibits a clear negative correlation with their fractions, i.e., increased distortion corresponds to reduced content. Specifically, the distortion of S444 first decreases and then increases with density, while its fraction correspondingly first increases and then decreases; in contrast, the distortion of S555 first increases and then decreases, with its fraction showing the opposite trend. By comparison, P(β) does not exhibit a similar pattern, as the out-of-plane distortion increases monotonically with density.

These findings indicate that in-plane distortion (γ), rather than out-of-plane distortion (β), plays a dominant role in regulating CNS stability and fraction distribution. As the in-plane distortion increases, the corresponding distortion energy $E_{distortion}$ (S) rises, making it more difficult for a given CNS to maintain its original structure and promoting transformation into other configurations. This process leads to competition among different CNS types and results in the observed oscillatory behavior of their fractions.

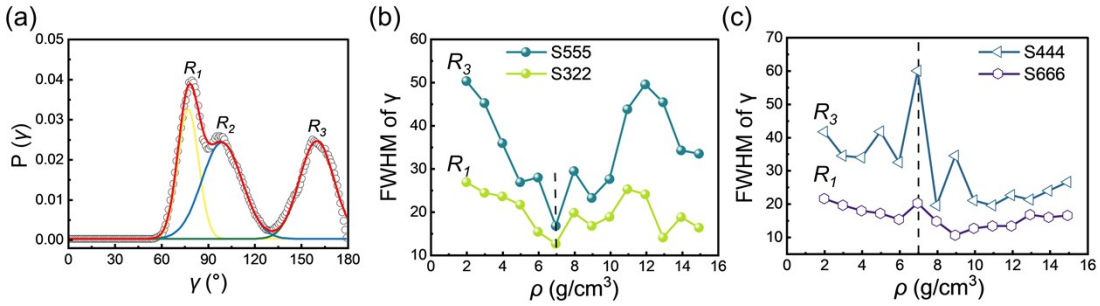

Figure S10. (a) P(γ) into three Gaussian subpeaks for S444 at 15 g/cm³; (b) variation of the full width at half maximum (FWHM) with density for S555 and S322; (c) variation of the FWHM with density for S444 and S666.

To further quantify this relationship, P(γ) was fitted using a Gaussian function (**Fig. S10(a)**), and the full width at half maximum (FWHM) was used to characterize the degree of in-plane distortion (**Fig. S10(b–c)**). The results further confirm that, over the entire density range, the oscillation of FWHM for the major CNS types shows a pronounced negative correlation with their fraction oscillations (e.g., for S555, the FWHM reaches maxima at 8 and 12 g/cm³, where the corresponding fraction attains minima).

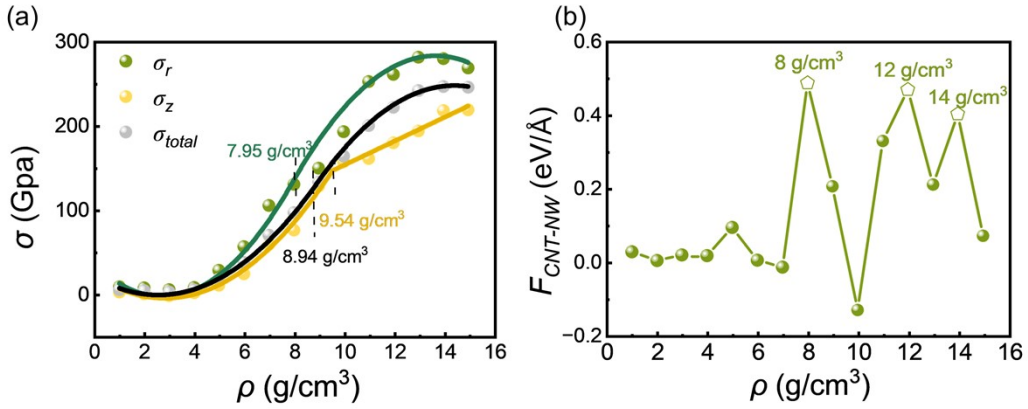

Figure S11. (a) Evolution of radial stress σ_r, axial stress σ_z, and total stress σ_{total} of the nanowire as a function of density; (b) Radial interaction force between the CNT and the nanowire, F_r.

Fig. S11(a) shows the variations of radial stress (σ_r), axial stress (σ_z), and total stress (σ_{total}) as functions of density. The results indicate that all three components increase monotonically with increasing density, suggesting that the system remains in a continuously enhanced compressive state. On this basis, the total interaction force between the CNT and the nanowire (NW) is projected onto the center line direction to obtain the radial interaction force, defined as $F_r = F \cdot \hat{r}$, as shown in **Fig. S11(b)**. The results reveal that F_r exhibits pronounced oscillatory behavior with increasing density.

Further analysis indicates that the F_r is the key driving factor for the structural distortion of CNS. However, due to differences in geometric adaptability, different CNS types exhibit markedly distinct responses to this radial interaction. Specifically, CNS such as S555 and S322 show a significant increase in in-plane distortion under stronger radial interaction, accompanied by reduced structural stability. In contrast, CNS such as S444 and S666 exhibit decreased in-plane distortion under the same conditions, demonstrating superior adaptability and stability under confinement. As a result, highly distorted CNS tend to transform into configurations with lower distortion, which ultimately leads to the observed oscillatory behavior in CNS fractions.

6. Additional angular distributions

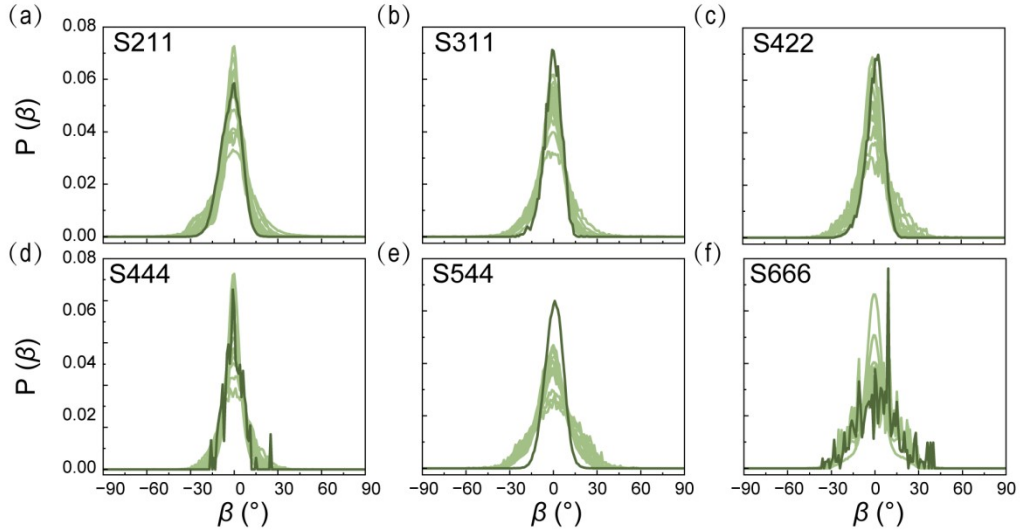

Figure S12.In-plane distortion distributions P(β) for S211(a), S311(b), S422(c), S444(d), S555(e) and S666(f), respectively.

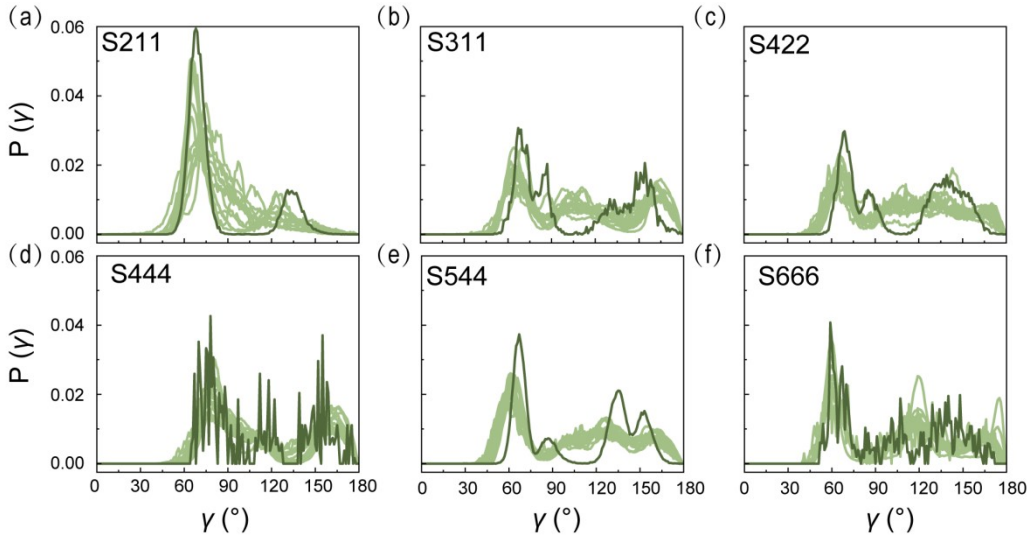

Figure S13.Out-plane distortion distributions P(γ) for S211(a), S311(b), S422(c), S444(d), S555(e) and S666(f), respectively.

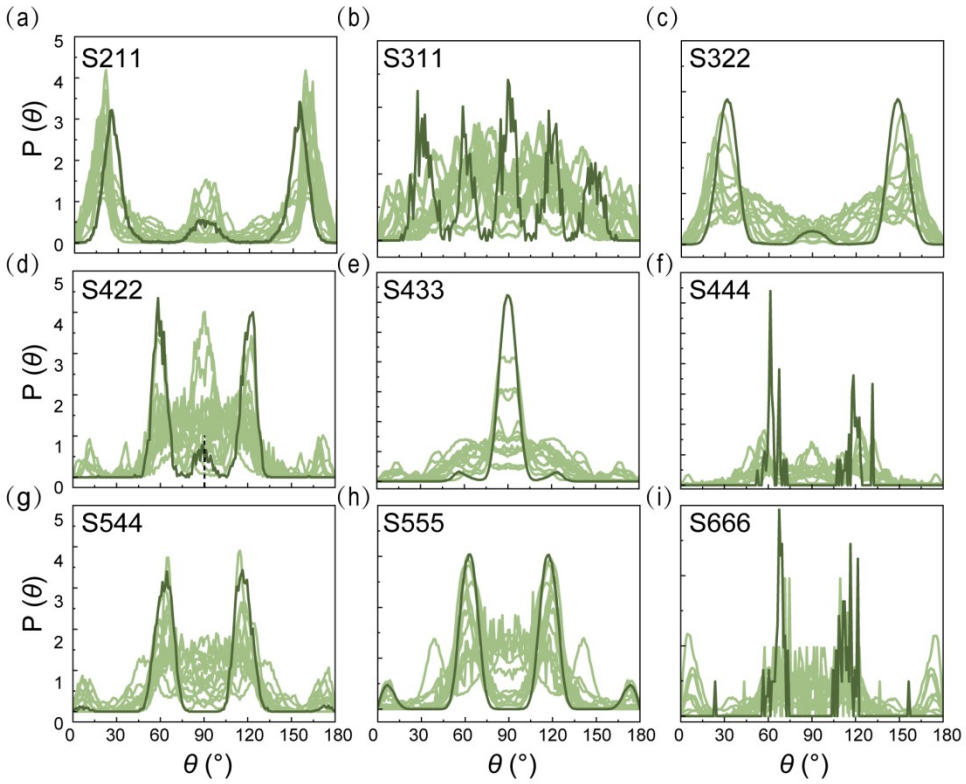

Figure S14. P(γ) for S211(a), S311(b), S322(c), S422(d), S433(e) and S444(f), S544(g), S555(h), S666(i), respectively.